

Representation of iron aerosol size distributions of anthropogenic emissions is critical in evaluating atmospheric soluble iron input to the ocean

Mingxu Liu^{1,2}, Hitoshi Matsui¹, Douglas Hamilton³, Sagar Rathod⁴, Kara Lamb⁵, Natalie Mahowald⁶

¹Graduate School of Environmental Studies, Nagoya University, Nagoya, Japan

²College of Environmental Science and Engineering, Peking University, Beijing, China

³Department of Marine, Earth, and Atmospheric Sciences, North Carolina State University, Raleigh, NC, USA

⁴La Follette School of Public Affairs, University of Wisconsin-Madison, Madison, WI, USA

⁵Department of Earth and Environmental Engineering, Columbia University, New York, NY, USA

⁶Department of Earth and Atmospheric Science, Cornell University, Ithaca, NY, USA

Correspondence to: [M.L. \(liumingxu@pku.edu.cn\)](mailto:liumingxu@pku.edu.cn) and [H.M. \(matsui@nagoya-u.jp\)](mailto:matsui@nagoya-u.jp)

Abstract. Atmospheric aerosol deposition acts as a major source of soluble (bioavailable) iron in open ocean regions where it limits phytoplankton growth and primary production. The aerosol size distribution of emitted iron particles, along with particle growth from mixing with other atmospheric components, is an important modulator of its long-range transport potential. There currently exists a large uncertainty in the particle size distribution of iron aerosol, and ~~the role of aerosol size in the extent to which such uncertainty~~ shapes ~~ing~~ global soluble iron deposition ~~is thus remains~~ unclear. ~~In this study~~ ~~Here~~, we couple a sophisticated microphysical, size-resolved aerosol model with an iron-speciated and -processing module to disentangle the impact of iron emission size distributions on soluble iron input to the ocean, with a focus on anthropogenic combustion and metal smelting sources. We ~~first~~ evaluate our model results against a global-scale flight measurement dataset for anthropogenic iron concentration and ~~find show~~ that the different representations of iron size distribution at emission, as adopted in previous studies, introduces a variability in modeled iron concentrations over remote oceans of a factor of 10. ~~S~~ ~~Shifting~~ ~~ing~~ the iron aerosol size distribution toward finer particle sizes ($<1 \mu\text{m}$) enables longer atmospheric lifetime (a doubling), promoting atmospheric processing that enhances the soluble iron deposition to ocean basins by up to 50% on an annual basis. ~~Importantly,~~ ~~The~~ monthly enhancements reach 110% and 80% over the Southern Ocean and North Pacific Ocean, respectively. ~~Uniquely,~~ ~~our results highlight that~~ ~~C~~ compared with emission flux ~~variability uncertainties, we find that~~ iron emission size distribution plays an equally important role in regulating soluble iron deposition, especially to the remote oceans. Our ~~new~~ findings ~~can help to interpret inter-model differences in iron deposition estimation and provide implications for to better quantify understanding~~ the effects of atmospheric nutrients input on marine biogeochemistry, including but not limited to iron, phosphorus, and others.

30 1. Introduction

31 Iron is a critical micronutrient supporting marine primary production, which is closely associated with marine carbon-nitrogen
32 cycles in the Earth system (Mahowald et al., 2018; Moore et al., 2001). The atmospheric deposition of soluble iron to many
33 ocean basins has long been regarded as an important source of bioavailable iron for ocean biota uptake in iron-limited areas
34 (Jickells et al., 2005; Jickells and Moore, 2015; Tagliabue et al., 2017). Understanding the amount and past-to-future evolution
35 of atmospheric iron deposition to the ocean is critical in assessing the ocean carbon sequestration under a changing climate
36 (Bergas-Massó et al., 2023; Myriokefalitakis et al., 2020; Hamilton et al., 2020b).

37 The quantification of soluble (bioavailable) iron input to the ocean is linked to differences in iron emission source properties,
38 the degree to which iron aerosol undergoes acidic or organic chemistry, and atmospheric transport (Hamilton et al., 2022).
39 Atmospheric iron comes from three major emission sources, i.e., wind-blowing dust, wildfire and biomass burning, and
40 anthropogenic activities, such as fossil fuel combustion and iron smelting. Dust storms, which frequently occur in arid or semi-
41 arid regions of the world, such as North Africa and East Asia, provide an abundant iron source to the ocean and support primary
42 production (Mahowald et al., 2009; Westberry et al., 2023). In addition, a growing body of evidence is showing that pyrogenic
43 iron, with higher fractional solubility than dust (Ito et al., 2019), is a large source of atmospheric soluble iron deposition to
44 many ocean basins, including the Southern Ocean, Northern Pacific Ocean, and Northern Atlantic Ocean (Conway et al., 2019;
45 Liu et al., 2022; Matsui et al., 2018; Seo and Kim, 2023). Because the strength of each source could be affected by future
46 climate change and/or human activities, their contributions to bioavailable iron input to the ocean may vary regionally and
47 temporally by the end of the century (Bergas-Massó et al., 2023).

48 Atmospheric transport provides the essential pathway in which iron aerosol emitted from the land is supplied to the remote
49 ocean. Atmospheric circulation patterns dictate the main transport pathways for aerosol to follow and thereby which source
50 regions are important to consider in terms of their supply to ocean basins. Additionally, atmospheric transport enables internal
51 mixing of iron-bearing aerosols with other aerosol and gas components, like sulfates and organics; a process commonly known
52 as aging that facilitates the dissolution of iron from an insoluble state to a soluble state (Shi et al., 2020; Shi et al., 2012;
53 Solmon et al., 2009; Li et al., 2017). The atmospheric aging processes can significantly increase iron solubility and subsequent
54 soluble iron deposition, evidenced by both in-field and laboratory observations and global model simulations (Ito, 2015; Li et
55 al., 2017; Longo et al., 2016). Uncovering the underlying mechanisms of the aging processes and associated enhancement of
56 iron solubility during transport is an ongoing topic of investigation (Meskhidze et al., 2019; Shi et al., 2020).

57 To elucidate atmospheric flux of iron-containing aerosols to the ocean, ~~atmospheric~~global-scale aerosol models have been
58 developed to include a range of iron emission sources that currently show a large intermodal difference in flux estimates
59 (Myriokefalitakis et al., 2018). Part of the problem is that it is difficult to realistically reproduce the distribution of soluble iron
60 concentrations across all the different regions of the world, and especially over the remote polar oceans that are often
61 characterized by low iron concentrations with a high fractional solubility (Ito et al., 2019). Among those global aerosol
62 simulations, Note that the size distribution of iron, which is an important consideration when determining ~~the particle~~aerosol
63 lifetimes; and thus its long-range transport potential, is key in shaping atmospheric iron ~~flux to the ocean~~distributions
64 (Hamilton et al., 2020a; Myriokefalitakis et al., 2018). Compared to coarse-sized particles (e.g., larger than 1 μm), smaller
65 particles generally feature lower loss rates with respect to dry deposition and wet removal, resulting in longer atmospheric
66 lifetimes; being transported a longer distance increases the potential for atmospheric processing (i.e., longer period of aerosol
67 ageing) and thus higher soluble iron deposition. Evidence from recent works (Zhang et al., 2023; Zhang et al., 2022) pointed
68 out that Fe sources and physicochemical properties largely differ between coarse and fine particles, leading to different Fe
69 solubility. Representation of iron size distribution in models could be therefore important.

70 Iron aerosol characteristics depend in part on differences between source types. The iron mass size distribution associated with
71 natural dust sources commonly pertains to mineral dust aerosols, with the coarse-sized (diameter greater than 1 μm) fraction
72 dominant (Mahowald et al., 2014; Albani et al., 2014). Similarly, fire iron emissions are dominated (>80%) by coarse mode
73 particles (Hamilton et al., 2019), suggested to be due to the entrainment of local dust iron-bearing aerosol in the pyro convective
74 updrafts generated by a fire (Hamilton et al., 2022). For iron aerosol with an anthropogenic source, however, the relative
75 fractions between the fine and coarse particle size distribution at emission are more divergent among previous investigations.
76 Recent observational constraints reveal large mass concentrations of anthropogenic iron oxide in the fine mode (Moteki et al.,
77 2017), while a subset of modelling studies have treated most of this iron in the coarse mode (Wang et al., 2015). As opposed
78 to those natural sources, anthropogenic iron size distributions may be highly variable with respect to diverse fuels, combustion
79 temperatures, and industrial processes, as well as the abatement technologies applied to control air pollution (Rathod et al.,
80 2020; Hamilton et al., 2020a).

81 The extent to which iron aerosol size distributions shape the pattern of atmospheric soluble iron inputs to different ocean
82 regions is currently unknown. Herein, by leveraging a size-resolved global aerosol model configured with iron processes, we
83 focus on the representation of anthropogenic iron size distributions at emission, primarily involving its roles in altering global
84 long-range transport and deposition fluxes of iron. We further put the effect of iron size distribution in the context with iron
85 emission uncertainty to shed light on their relative importance in controlling global-scale iron deposition.

86

87 **2. Methods and Materials**

88 **2.1 Global aerosol model**

89 We conducted global aerosol simulations using the Community Atmospheric Model version 5 (CAM5.3) with the Aerosol
90 Two-dimensional bin module for foRmation and Aging Simulation version 2 (CAM-ATRAS) (Matsui, 2017; Matsui and
91 Mahowald, 2017). The model treats a series of aerosol chemical and microphysical processes in a size-resolved manner with
92 12 aerosol size bins from 1 to 10,000 nm in diameter. Our recent study suggests that this size-resolved method can well
93 represent the growth of small particles to larger ones and the evolution of particle size distributions during atmospheric
94 transport (Liu and Matsui, 2022). Both dry deposition (Zhang et al., 2001) and wet deposition (Liu et al., 2012) of aerosols are
95 treated in our model. The improvement of aerosol in-cloud wet scavenging process was included to improve the modelling of
96 aerosol long-range transport efficiency (Liu and Matsui, 2021). The CAM-ATRAS model has been adequately validated for
97 aerosol mass and number concentrations at a global scale using comprehensive measurements from the ground to the upper
98 troposphere (Matsui and Liu, 2021; Gliš et al., 2021; Kawai et al., 2021; Matsui et al., 2022; Matsui and Moteki, 2020).

99 To represent the iron cycle from emission to deposition, we explicitly treated iron constituents within the aerosol model, similar
100 to our previous study (Liu et al., 2022), while with updates for iron processing in the current work. All iron-bearing components
101 were assumed to be internally mixed with other aerosols and underwent emission, physical transport, chemical aging (e.g.,
102 solubilization), and deposition in the atmosphere. The internal mixing assumption is reasonable for anthropogenic iron aerosols,
103 which are often mixed together with other aerosol compounds in the polluted environments, e.g., East Asia, and enable the
104 growth of iron aerosols via condensation and coagulation. Our model simulated iron solubility and atmospheric processing of
105 iron-bearing aerosols through the online coupling with the Mechanism of Intermediate complexity for Modelling Iron
106 (Hamilton et al., 2019). For anthropogenic iron, we consider five different minerals, namely magnetite, hematite, illite,
107 kaolinite, and sulfate iron, following the global emission inventory by Rathod et al. (2020), which was developed by a bottom-
108 up approach at 1° spatial resolution and 1-month temporal resolution-. The reference year of the inventory was 2010. We

109 account for a wide range of anthropogenic sources including iron smelting and fossil fuel combustion sources ~~taken into~~
110 ~~account~~.

111 Dust iron emission was calculated by assuming a constant iron content of 3.5% in dust aerosol emission (Shi et al., 2012). ~~The~~
112 ~~model estimated total dust emission fluxes using the scheme of~~ Zender et al. (2003), ~~with modifications by~~ Albani et al. (2014)
113 ~~and the size distribution from~~ Kok (2011). ~~Dust mineralogy was not involved in our simulations.~~ The global interannual mean
114 iron (insoluble + soluble) emissions from dust, biomass burning, and anthropogenic sources were 87 Tg Fe yr⁻¹, 1.1 Tg Fe yr⁻¹,
115 and 2.2 Tg Fe yr⁻¹, respectively.

116 We validated our modeled anthropogenic iron oxide concentrations against a global-scale aircraft measurement in the
117 troposphere consisting of eight campaigns for the periods of 2009–2011 and 2016–2018 (Lamb et al., 2021). These
118 observations ~~provide~~~~include~~ mass concentrations of anthropogenic iron oxide, i.e., magnetite aerosols, ~~with~~~~with~~ volume
119 equivalent diameters between 180–1290 nm. The model results were extracted along the flight tracks in time and space and
120 further averaged in several latitudinal bands across Pacific and Atlantic Oceans (see Fig. S1). More details can be seen in Liu
121 et al. (2022).

122 The model was compiled with a horizontal resolution of 1.9° × 2.5° (latitude × longitude) and 30 vertical layers from the
123 surface to 40 km. We ran the model for the two periods, 2008–2011 and 2015–2018, with the first year in each period as spin-
124 up. The meteorological fields were nudged by the Modern-Era Retrospective analysis for Research and Applications Version
125 2. In addition, to provide implications for ocean biogeochemistry, we estimated the changes in marine net primary production
126 induced by iron inputs following the methods used by Rathod et al. (2022) and Okin et al. (2011), in which a cut-off (4 μmol
127 L⁻¹) of nitrate concentrations at surface water was chosen to define the geographical areas of iron-limited ocean basins.

128 **2.2 Representation of iron size distribution of anthropogenic emissions**

129 The number and mass size distribution of aerosol at emission is an essential parameter in aerosol modelling. However, due to
130 the limited knowledge about iron emission characteristics, the representation of iron size distributions varies greatly for
131 anthropogenic sources. We tested four different size distributions of anthropogenic iron at emission (Fig. 1), briefly described
132 as follows.

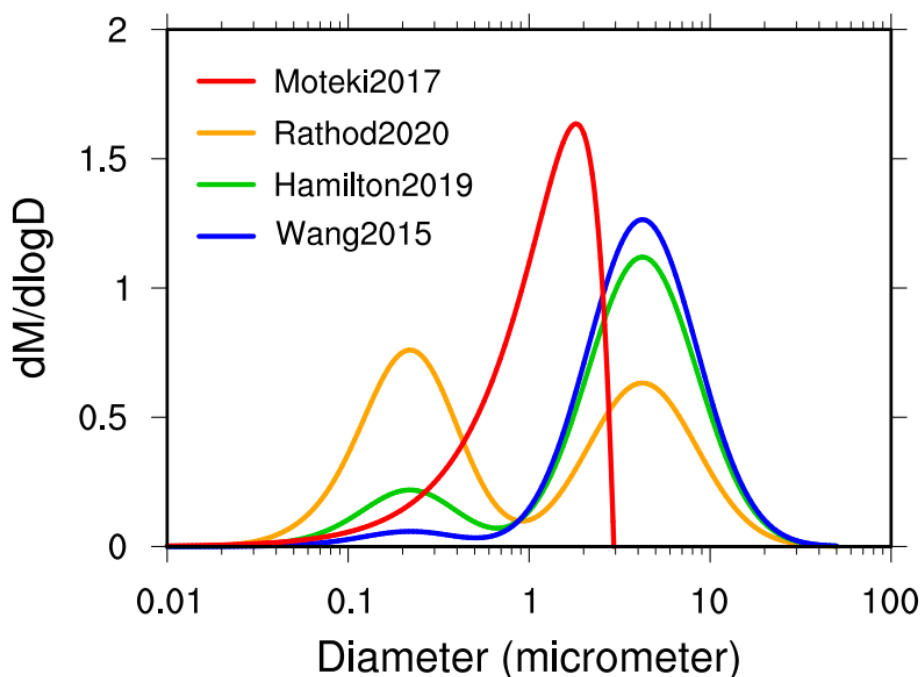
133 First, we adopted the same size distribution with our previous studies (Matsui et al., 2018; Liu et al., 2022) based on Moteki
134 et al. (2017), abbreviated as Moteki2017 hereafter, which was derived from a power law function to fit the observed
135 anthropogenic iron oxides concentrations within the boundary layer in the outflow of East Asian sources. Note that the
136 observed size-resolved number concentrations were confined within 170 to 2,100 nm in diameter given the detection limit. By
137 extrapolating the observation results, we obtained the mass size distribution between 1 nm and 10,000 nm with negative values
138 excluded. In this case, more than 90% of iron mass was allocated to the size range of 100 nm to 2,500 nm. In addition, we
139 varied the emissions by a factor of two (×0.5 and ×2.0, respectively) in another two parallel experiments to account for the
140 potential uncertainties in iron emission estimates.

141 The second case was derived from Rathod et al. (2020) (abbreviated as Rathod2020 hereafter). They developed a new
142 mineralogy-based iron emission inventory by introducing more details in anthropogenic sources, especially the inclusion of a
143 metal smelting source. These improvements increase the fine aerosol (less than 1 μm in diameter) fractions by a factor of 10
144 higher than most previous inventories. Consequently, this inventory was characterized with almost equal fractions between
145 fine- and coarse-sized emissions, while previous inventories always applied a much larger fraction for the coarse mode.
146 Consistent with Rathod et al., we allocated 10% and 90% of fine iron mass to the Aitken mode and the accumulation modes
147 of aerosols, respectively.

148 The third case was derived from Hamilton et al. (2019) (abbreviated as Hamilton2019 hereafter). They revised the
149 anthropogenic iron emission inventory based on Luo et al. (2008) (no metal smelting) and showed that the ratio of fine-sized
150 iron mass with that of the coarse-sized was 1:5.6, which resulted in the coarse mode dominating. A similar ratio for
151 anthropogenic iron emissions was applied by Ito (2013). Also, 10% of fine-sized emissions were allocated to the Aitken mode
152 and the remaining 90% to the accumulation mode.

153 The fourth case was derived from Wang et al. (2015) (abbreviated as Wang2015 hereafter). In their combustion-iron inventory,
154 the ratio of fine-mode mass to the coarse mode was as low as 1:24, because only 0.1–0.3 % of iron mass from coal fly ash
155 were emitted in the fine mode. Thus, we allocate 96% of iron in the coarse mode and the remaining 4% in the fine mode.

156 To enable the intercomparison among these cases, we used the global-scale anthropogenic iron emission mass inventory from
157 Rathod et al. (2020) but with different allocations between fine and coarse sizes in each case. The size distribution of
158 anthropogenic iron emission in each case was treated uniformly on a global scale. Therefore, the simulated variability in
159 atmospheric iron input to the ocean between cases should be attributable to iron size distributions rather than emission amount.
160 For the last three cases, we adopted three constant log-normal modes to distribute iron emissions, namely Aitken, accumulation,
161 and coarse modes, with their determining parameters including geometric standard deviations, number mode diameter, and
162 density reported by Hamilton et al. (2019). We then separated these three modes into 12 size bins from 1 nm to 10,000 nm
163 adapted for our size-resolved aerosol modelling. The size distributions of iron from biomass burning and dust sources were
164 consistent with Liu et al. (2022) in all cases. In the following analysis, we grouped the Moteki2017 and Rathod2020 as the
165 fine-sized group while the Hamilton2019 and Wang2015 as the coarse-sized group.



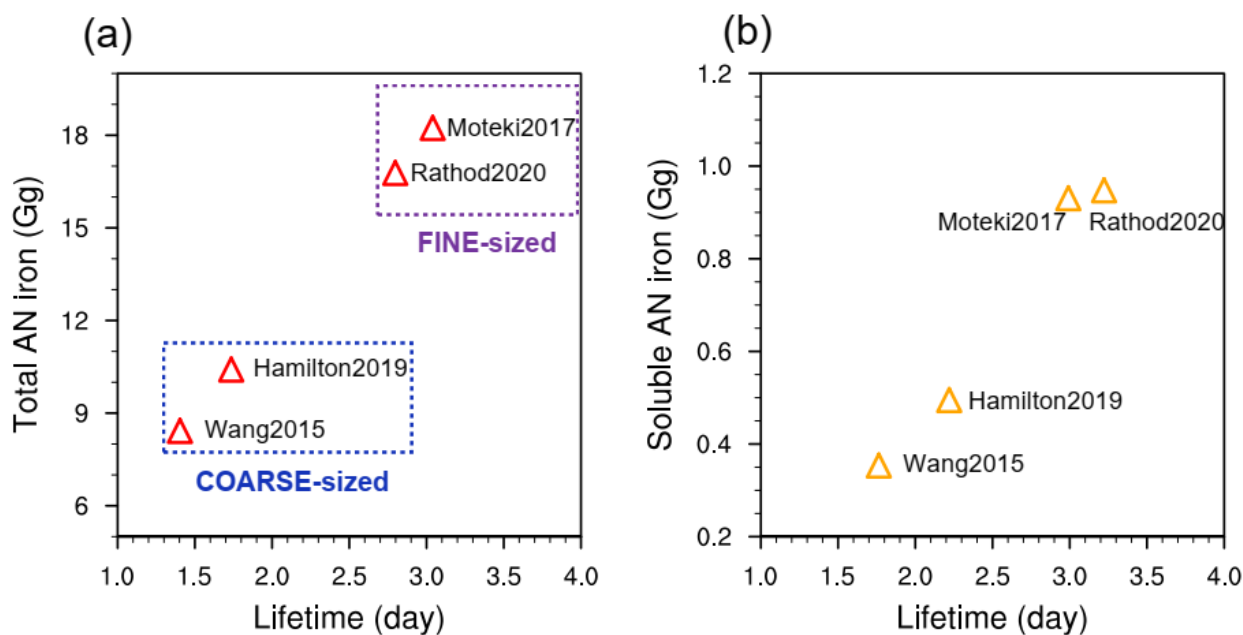
166
167 **Fig. 1.** Mass size distribution functions for anthropogenic iron emission adopted in four previous studies. The Moteki2017
168 curve was provided by fitting in-situ measurements for iron particles within the range of 170 and 2,100 nm in diameter over
169 East Asia; the Rathod2020 was based on the latest combustion iron emission inventory, with updates on iron estimate in fine-
170 mode sizes (<1 μ m); the Hamilton2019 and Wang2015 cases were modeling studies that assumed most anthropogenic
171 combustion in the coarse-mode bin.

172

173 3. Results and Discussion

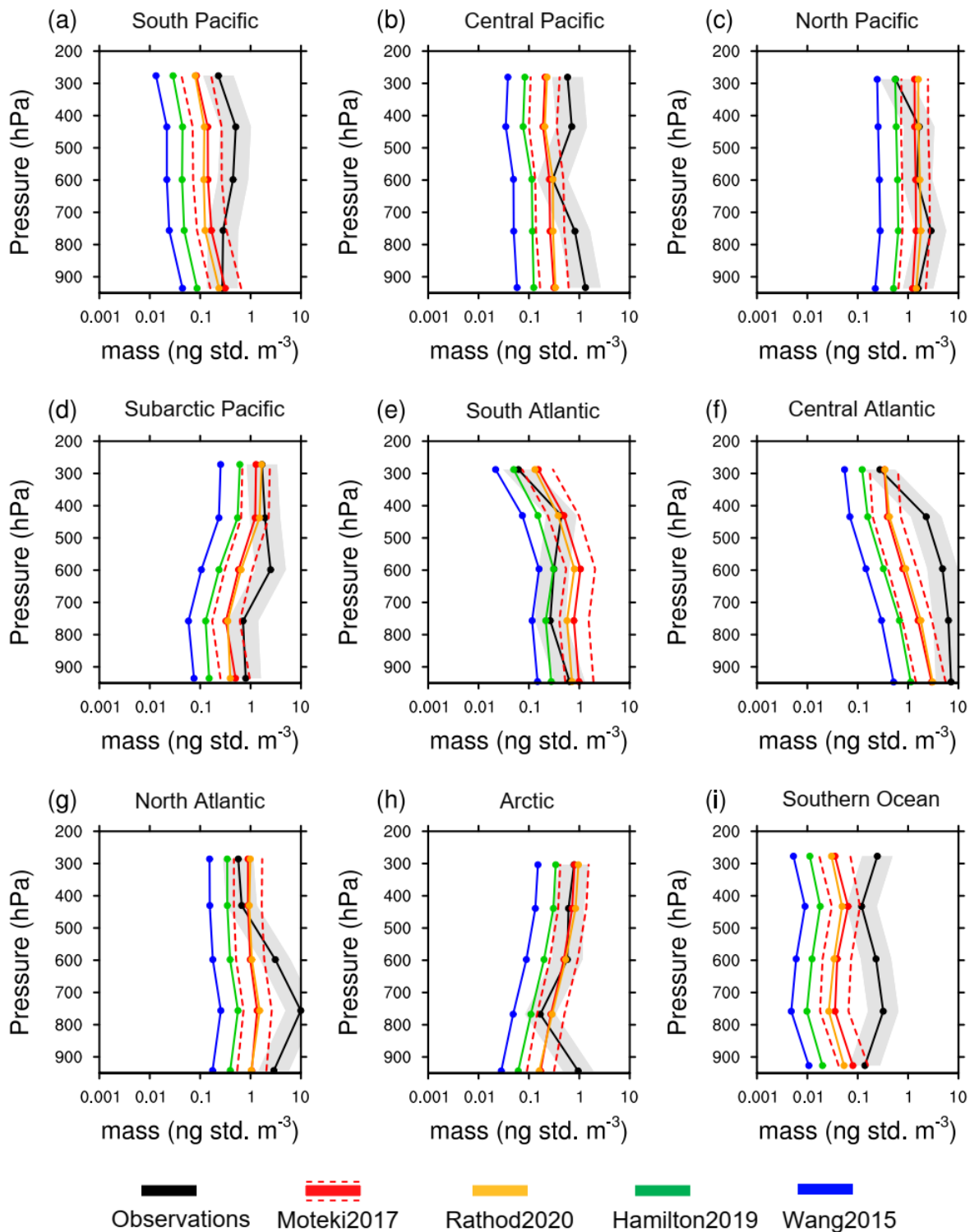
174 3.1 Atmospheric iron aerosol concentrations

175 We first examined the effect of changes to iron particle size distributions for anthropogenic sources (unless otherwise stated)
 176 on the atmospheric iron aerosol burden and its global distributions. Figure 2 illustrates that the global-mean anthropogenic
 177 iron lifetimes differ by about a factor of 2 among the four examined cases. Both the Moteki2017 and Rathod2020 cases
 178 simulated a lifetime around 3.0 days. In contrast, the Hamilton2019 and Wang2015 cases simulated a lifetime around half as
 179 long (between 1.4 and 1.7 days). As only the size distribution is changed in these simulations the change in lifetime is directly
 180 linked to the apportionment of mass aerosol between fine and coarse particle size modes. This result is in line with previous
 181 reports (Hamilton et al., 2020a), and demonstrates that shifting emitted iron toward fine-sized diminishes atmospheric loss
 182 rates of iron aerosols via dry (sedimentation) and wet (precipitation) removal pathways and extends their lifetime.
 183 Consequently, given the same emission amount, the atmospheric iron burdens are enhanced, accordingly by approximately a
 184 factor of 2 from ~9.0 Gg in the coarse-sized cases (Hamilton2019 and Wang2015) to ~18.0 Gg in the fine-sized cases
 185 (Moteki2017 and Rathod2020). In a similar manner, the lifetimes and mass burdens of anthropogenic iron in the soluble form
 186 are almost doubled in the fine-sized cases (Fig. 2b). The extended lifetimes also enhance the globally averaged iron solubility
 187 (Fig. S2), by allowing more iron subject to aerosol aging and solubilization processes.



188
 189 **Fig. 2.** Global anthropogenic iron concentration burdens and lifetimes varied by the emission size distributions. The scatter
 190 plots are shown for (a) anthropogenic iron (labeled as AN iron) burden vs. lifetime and (b) soluble anthropogenic iron vs.
 191 lifetime. Four representative cases are examined in this work: Moteki2017, Rathod2020, Hamilton2019, and Wang2015. The
 192 first two cases are grouped into “FINE-sized” and the other two are grouped into “COARSE-sized”.

193



194

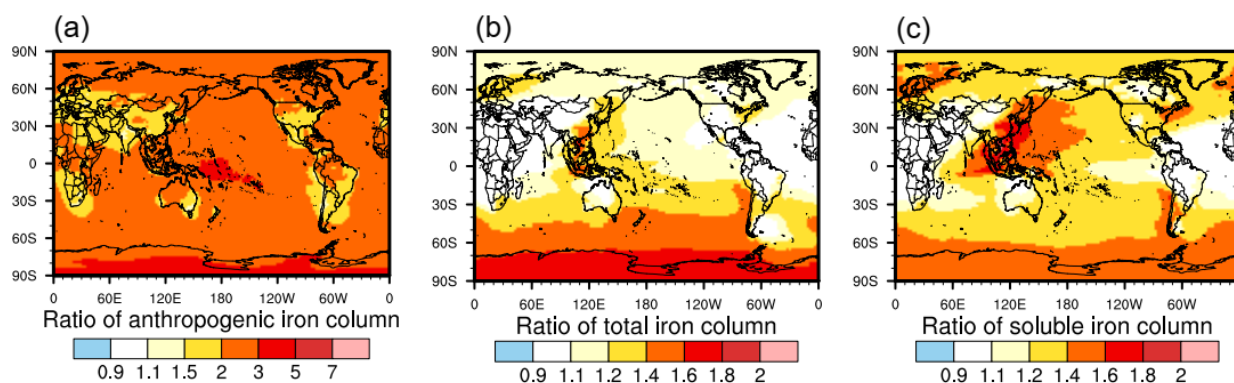
195 **Fig. 3.** Comparison of modelled anthropogenic iron mineral (magnetite) vertical concentration profiles in four cases with
 196 aircraft measurements across global oceans. The flight routes and model-observation sampling methods have been documented
 197 in Lamb et al. (2021) and Liu et al. (2022). The geographical location of each oceanic area is marked in Fig. S1. We also scaled
 198 up and down emission fluxes by a factor of 2 from the Moteki2017 case, respectively, to account for potential uncertainties in
 199 emission estimates (red dashed lines in the panels).

200 To evaluate each iron simulation, we compare simulated aerosol characteristics against global-scale aircraft measurements of
 201 anthropogenic magnetite within nine regions of the troposphere (Fig. 3). We extracted the modeled mass concentrations of
 202 iron aerosols with The size the size distribution range similar -consistent with to that of the measurements -is selected for our
 203 model results. Note that magnetite, comprised about 70% of anthropogenic iron emissions, can be used as an indicator of
 204 anthropogenic iron abundance in the atmosphere (Rathod et al., 2020; Matsui et al., 2018). Despite the same emission fluxes
 205 considered in all cases, their simulated magnetite aerosol concentrations can differ by up to a factor of 10. Specifically, the

206 Moteki2017 and Rathod2020 cases show a much higher performance in reproducing the observed profiles over all ocean basins
 207 compared to Hamilton2019 and Wang2015 cases. In particular, the cases with a more uniformly distributed particle size
 208 distribution across modes captures the high concentration ($>1 \text{ ng m}^{-3}$) in North Pacific, which can be linked to atmospheric
 209 plumes transported from East Asia with intensive emission rates (Seo and Kim, 2023; Moteki et al., 2017). Some
 210 underestimations still exist in near-surface or high altitudes. Doubling the emission fluxes based the Moteki2017 case can
 211 appreciably narrow the gaps with the observation (dashed red lines in Fig. 3). In contrast, the coarse-sized dominated
 212 simulations (i.e., Hamilton2019 and Wang2015) underrepresents the magnetite concentrations over global remote oceans,
 213 particularly by up to one order of magnitude over the Pacific Ocean. The shorter lifetimes in this group limit the long-range
 214 transport of iron aerosols from continental sources to the remote atmosphere.

215 These results imply that agreement between observations and model simulations can be improved by reducing uncertainties in
 216 the emission inventory and in the long-range transport efficiency associated with representation of iron size distributions.
 217 Moreover, as illustrated in Fig. 3, the variabilities (the ratio between the maximum and minimum) of simulated magnetite
 218 vertical profiles by iron size distribution changes are wider than those by the emission uncertainties, for which emission fluxes
 219 were perturbed by a factor of 2 ($\times 2.0$ and $\times 0.5$, respectively) to test the sensitivity of simulated iron concentrations. We
 220 therefore highlight that in order to observationally constrain iron emissions more realistically in global aerosol simulations, it
 221 is a prerequisite to use a realistic empirical representation of anthropogenic iron aerosol size distributions.

222



223

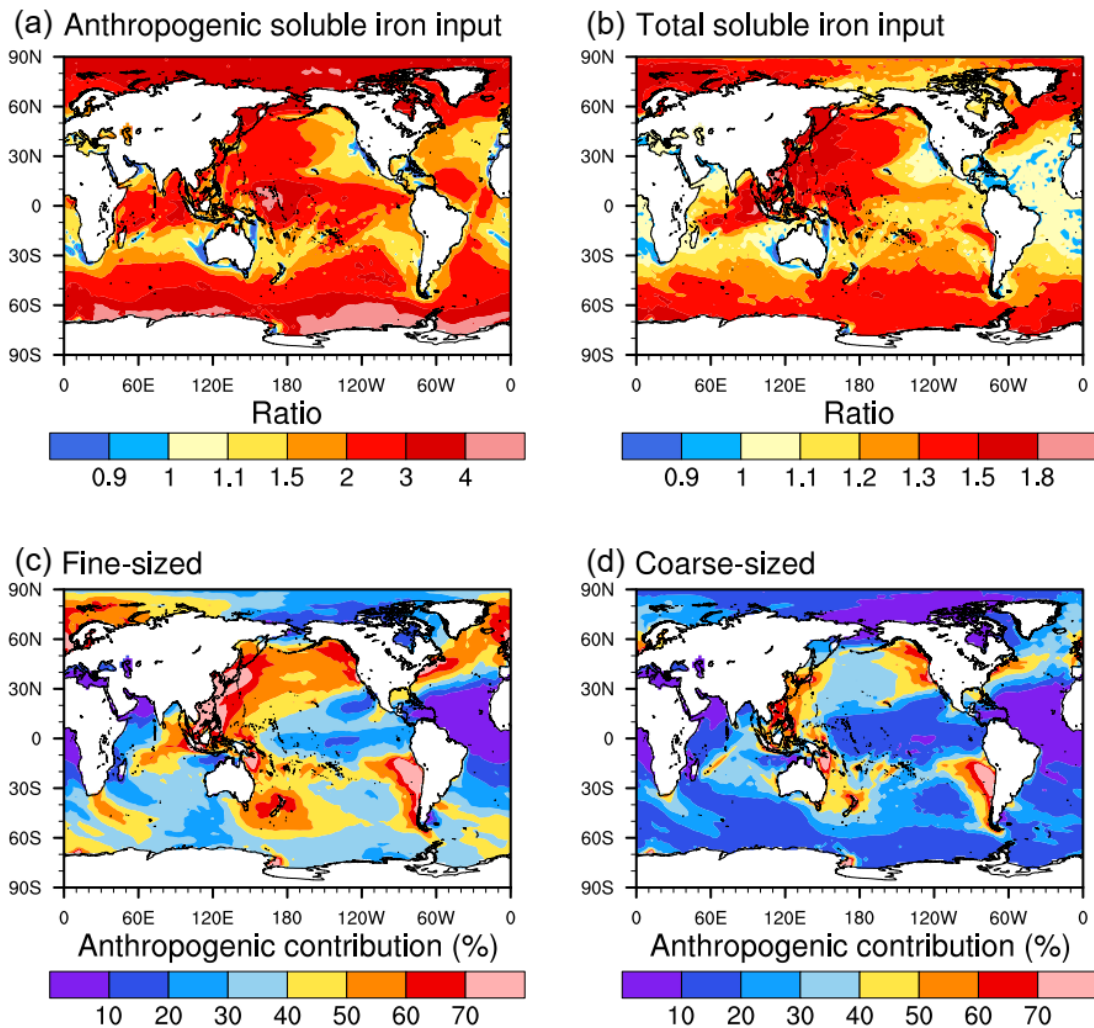
224 **Fig. 4.** Global map of variability in yearly averaged iron column concentrations between the fine-sized group and the coarse-
 225 sized group. The variability ratios (fine-sized/coarse-sized) are calculated for (a) anthropogenic iron, (b) total iron, and (c)
 226 soluble iron, respectively. Herein, total iron is a combination of iron from dust, biomass burning, and anthropogenic sources,
 227 the soluble form of which denotes soluble iron. The ratios represent the maximum differences between the fine-sized group
 228 (the Moteki2017 and Rathod2020 cases) and the coarse-sized group (the Hamilton2019 and Wang2015 cases) and indicate the
 229 spread of iron simulations.

230 Our simulations further demonstrate that the representation of iron size distribution shapes the iron aerosol concentrations at a
 231 global scale (Fig. 4). Anthropogenic iron in the fine-sized group shows higher column concentrations by more than a factor of
 232 2 than in the coarse-sized over oceans. The differences (ratios) are larger in those remote oceans compared to source regions
 233 like East Asia, southern Africa and South America, because iron-bearing aerosols in smaller sizes can be transported to a
 234 longer distance. The variability between the two groups is relatively much less minor relative to for total iron (Fig. 4b), which
 235 also includes contributions from dust and biomass burning sources. One exception is the Southern Ocean with still large ratios
 236 around 1.5, reflecting an important fractional contribution of anthropogenic iron among all sources over this region. By contrast,
 237 Note that the differences for soluble iron are more pronounced than for total iron over much of the global Ocean (Fig 4c),
 238 because of the higher solubility of anthropogenic iron than dust iron. Over East Asia and its outflow areas, the rapid aging
 239 process in the polluted environments are capable of enhancing iron solubility, particularly those of anthropogenic origin, and

240 thus amplify the differences of soluble iron concentrations between the fine-sized and coarse-sized groups (Li et al., 2017; Zhu
241 et al., 2022).

242

243 3.2 Atmospheric soluble iron input to the ocean



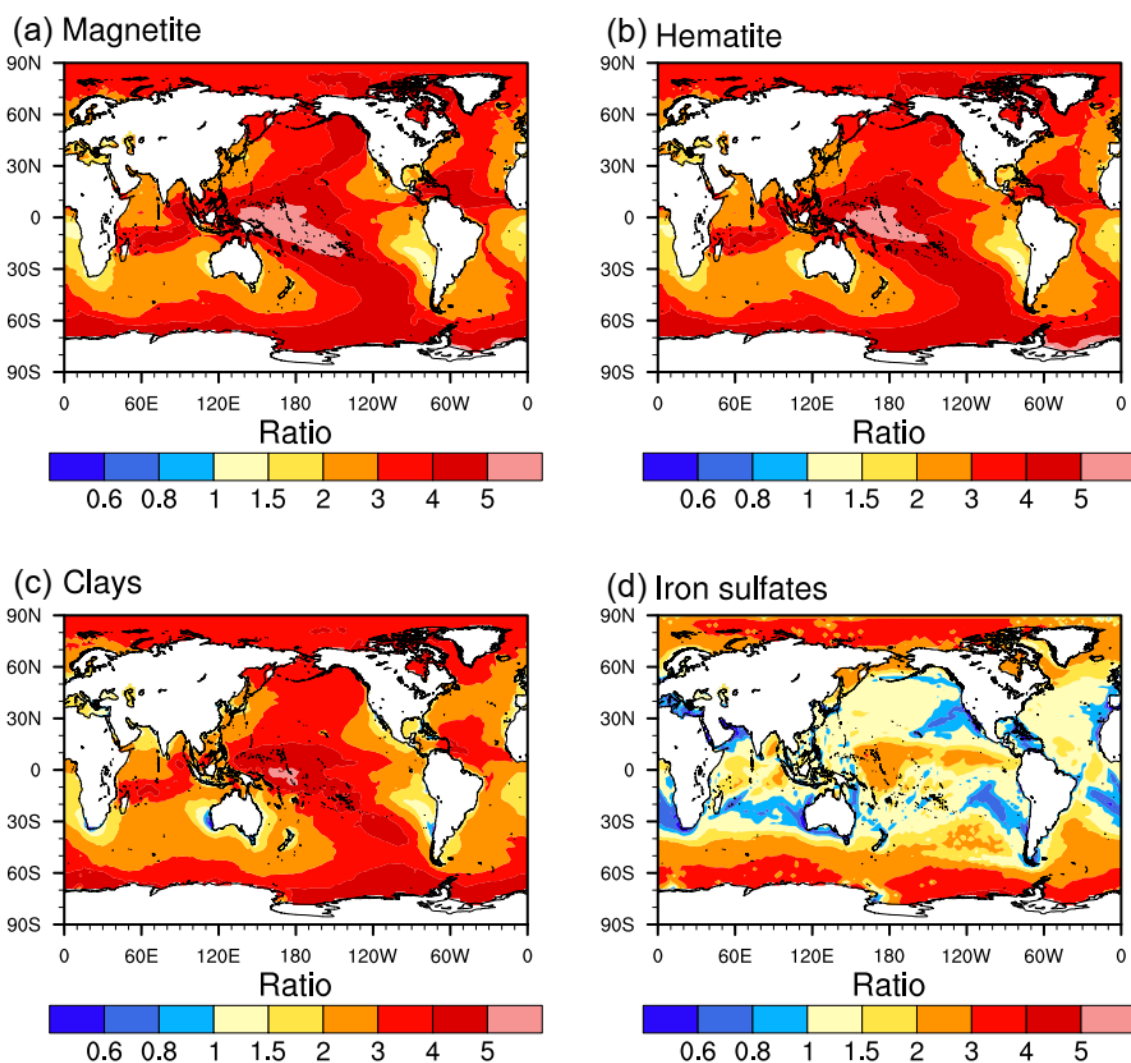
244

245 **Fig. 5.** Comparison of yearly accumulated atmospheric soluble iron input to the ocean between the fine-sized and coarse-sized
246 cases. Shown here are (a) the ratio of anthropogenic soluble iron simulated in the fine-sized case to the result of the coarse-
247 sized, (b) the ratio of total soluble iron, (c) the fractional contribution (in percentage) of anthropogenic emission to total soluble
248 iron input in the fine-sized case, and (d) the fractional contribution of anthropogenic emission in the coarse-sized case.

249 Next, we examine the extent to which the iron size distributions at emission can alter soluble iron input to the global ocean
250 basins, which is vital to net primary productivity, especially in the high-nutrient, low-chlorophyll (HNLC) areas (Hamilton et
251 al., 2022; Moore et al., 2013). As illustrated in Fig. 5, though the global emission and the resulting annual iron (insoluble +
252 soluble) deposition amount are the same between cases, their geographical distributions vary substantially. Using the ratio of
253 annual soluble iron deposition in the fine-sized group to that of the coarse-sized as a proxy of the variability, we find the fine-
254 sized distributions lead to much more soluble iron input to remote ocean basins including North Pacific and Southern Ocean,
255 by up to a factor of 4 for the anthropogenic sources and 1.5 for the total of all sources (i.e., anthropogenic + fire + dust). Similar
256 spatial patterns emerge regarding the total iron deposition, suggesting the importance of long-range transport efficiency in
257 regulating iron distributions (Fig. S3). The variability is negligible in the equatorial and subtropical Atlantic, where dust iron
258 dominates soluble iron input to this area. The ratios less than 1, indicating reduced deposition fluxes in the fine-sized group,
259 are found near the continental sources, including western U.S., Australia, and southern Africa, because of the slower deposition

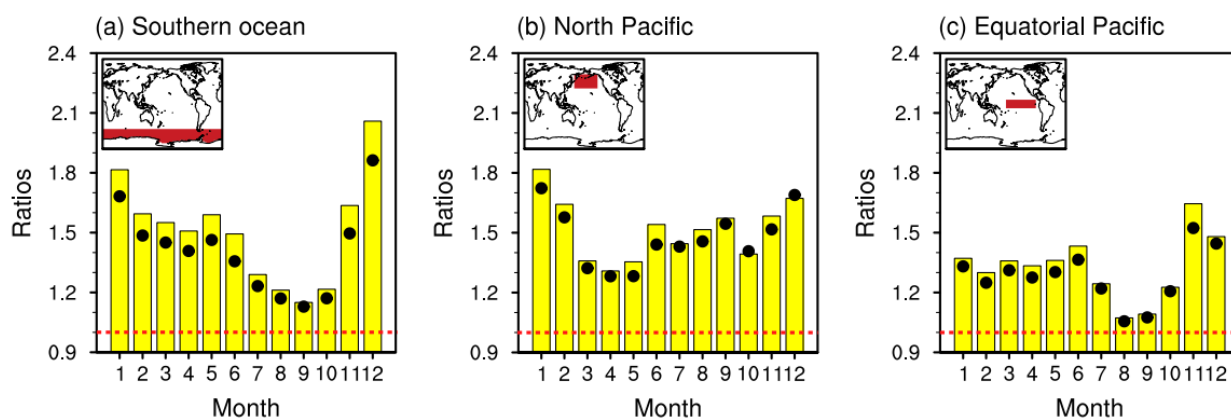
260 speed. However, in East Asia, which has most intensive anthropogenic iron emissions, the shift toward finer sizes also increase
 261 soluble iron deposition near the sources (e.g., eastern China). This is attributable to the rapid aging processes of the fine-sized
 262 iron in such polluted environment that convert more insoluble iron to its soluble form (Baldo et al., 2022; Zhang et al., 2022).

263 The source appointment of soluble iron deposition across ocean basins also varies with iron size distributions (Fig. 5c-d). The
 264 anthropogenic iron ~~sourceemission~~ becomes more dominant in North Pacific, North Atlantic, and parts of the Southern Ocean,
 265 with its fractional contribution reaching more than 50% in the fine-sized group compared to that of 30–40% in the coarse-
 266 sized. Such variability is attributable to the enhancement of anthropogenic soluble iron fluxes to those remote oceans by the
 267 shift of anthropogenic iron emission toward finer size bins. Globally, the soluble iron deposition from anthropogenic sources
 268 is 55.0 Gg per year for the fine-sized group, larger than that of 35.3 Gg per year for the coarse-sized group. Hence, even though
 269 the same emission is applied in these simulations, the diversity of iron size distributions at emission yields a considerable
 270 variability of soluble iron deposition on a global basis. As discussed earlier, the extended iron lifetime by about a factor to 2
 271 in the fine-sized group allows more iron to be transported to a remote region and simultaneously increases the amount of
 272 atmospheric iron processing and dissolution to a soluble form. Of the total iron deposition, the soluble fraction is thus notably
 273 elevated. We also find that the chemical aging process, as the major source of soluble iron, controls the differences of soluble
 274 iron deposition over remote oceans between the fine-sized and coarse-sized groups (Fig. S4).



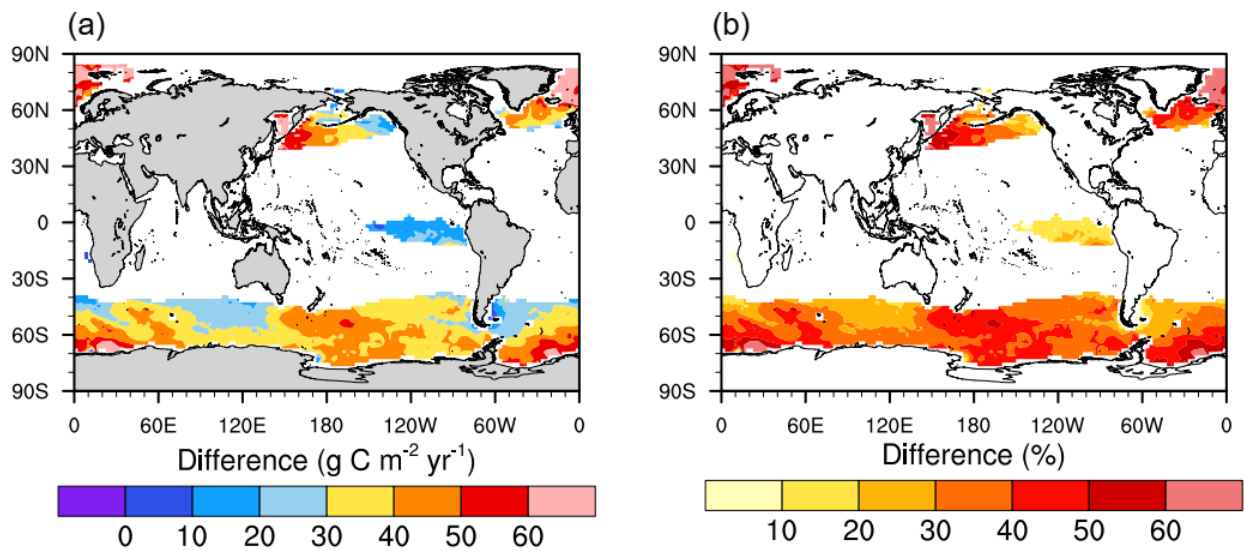
275
 276 **Fig. 6.** Ratios of yearly accumulated soluble iron deposition ~~for from~~ four anthropogenic iron-containing minerals, comparing
 277 between the fine-sized and coarse-sized cases.

278 In this study, the explicit treatment of anthropogenic iron mineralogy enables us to identify the iron mineral-dependent
 279 variability. We find that for those coming primarily from fossil fuel combustion and iron smelting on land, namely magnetite,
 280 hematite, and clays, the shift of iron emissions toward finer size bins promotes their long-range transport and enhances
 281 corresponding soluble iron deposition to North Pacific, Equatorial Pacific, and Southern Ocean by more than a factor of 4 (Fig.
 282 6a-c). However, the size distribution effects on iron sulfates are pronounced only in the polar areas, which are subject to plumes
 283 of middle latitude shipping emissions. In line with previous study (Rathod et al., 2022), the iron sulfates constitute an important
 284 contribution to soluble iron deposition away from major continental sources, predominately associated with shipping emission
 285 over local oceans rather than long-range transport from land (Fig. S5). Hence, the variability induced by iron size distributions
 286 is less remarkable for iron sulfates than for other anthropogenic minerals. These results also suggest that the relative importance
 287 of iron sulfates in total soluble iron deposition to remote oceans is altered by the size distributions of all other iron minerals
 288 that originate from continental sources. Because the size distributions of anthropogenic iron minerals may depend on different
 289 combustion processes, source- and region-specific size distribution representation is desirable in the future work.



290
 291 **Fig. 7.** Differences of monthly total soluble iron deposition between the fine-sized and coarse-sized groups over specific ocean
 292 basins. Only anthropogenic iron emission sizes have been examined here. Histograms describe the ratio of monthly results in
 293 the fine-sized case to that of the coarse-sized for (a) Southern Ocean, (b) North Pacific, and (c) Equatorial Pacific, respectively.
 294 For comparison, black dots describe the ratio of the fine-sized results to that with global anthropogenic emission amount
 295 scaling down by a factor of 2. The ocean basins of interest are indicated at the top-left corner of each panel. The red dashed
 296 lines indicate the ratio of 1.0.

297 It is critical to examine monthly soluble iron availability altered by emission size distributions, because ocean primary
 298 production can respond to iron inputs on the order of days to months (Guieu et al., 2014). From our results in Fig. 7, the
 299 importance of anthropogenic emission size distributions in shifting soluble iron deposition varies by month over potentially
 300 iron-limited ocean basins, i.e., HNLC regions, due to the episodic nature of natural iron sources (dust and wildfire) and their
 301 deposition. For the Southern Ocean, the monthly ratios of the fine-sized case to the coarse-sized span from 1.1 in September
 302 to 2.1 in December (Fig. 7a). The September peak of fire iron (shown in Fig. S6), possibly linked to low precipitation in
 303 southern winter, masks the variability in anthropogenic iron contributions by emission size distributions. Conversely, the
 304 largest difference in December is associated with the lowest contribution of natural sources (Fig. S6). By contrast, the monthly
 305 differences are less fluctuated in North Pacific, ranging between 1.3 and 1.8 (Fig. 7b). Anthropogenic emission dominates
 306 soluble iron throughout the year except in March-May, during which dust storms originating from East Asia frequently occur
 307 and regulate soluble iron inputs to North Pacific. The Equatorial Pacific has the lowest ratio amongst the three regions, because
 308 anthropogenic aerosol bearing plumes rarely arrive in this region and lots of rain out here can efficiently remove aerosols. For
 309 the three ocean basins, such differences related to the emission size treatments are even larger than those by adjusting the iron
 310 emission amount by a factor of 2 with the consideration of emission uncertainty (black dots in Fig. 7). We therefore suggest
 311 that compared with iron emission fluxes, the representation of size distributions for anthropogenic iron is equally or even more
 312 important to the estimation of total soluble iron deposition to remote oceans.



313

314

315

316

317

Fig. 8. Difference of marine net primary production sustained by atmospheric soluble iron between two iron size distribution groups. The panels display (a) absolute differences and (b) percentage differences in net primary production of the fine-sized group relative to the coarse-sized group. Here, following Rathod et al. (2022), we focus only on the iron-limited ocean basins, which are defined using a cut-off of nitrate concentrations at surface oceans.

318

319

320

321

322

323

324

325

326

327

328

329

330

331

332

333

334

335

336

337

338

339

340

341

342

We also provide an estimate of the changes in iron-sustained marine net primary production between the finer-sized and coarse-sized groups (Fig. 8). In line with the distributions of soluble iron deposition, the effects of finer-sized iron distributions can enhance primary production over remote oceans including the North Pacific Ocean and Southern Ocean as high as 50%. Considering that anthropogenic iron aerosols may contribute to >10% of the total marine productivity in the North Pacific Ocean (Rathod et al., 2022; Ito et al., 2020), the representation of their size distributions at emissions, mostly from East Asia, is particularly important in the Earth system modeling. The evolution of atmospheric iron-aerosol size characteristics and their emission fluxes can be critical players to ocean carbon sequestration from past to future. Hamilton et al. (2020) found that historical air pollution controls has cut down anthropogenic emission amounts of particles in coarse sizes, in turn elevating the mass fraction of finer-sized iron particles and thus the overall lifetime of atmospheric iron. Hence, the complex interactions of iron and the Earth system is linked to human activity effects on soluble iron availability to ocean basins.

4. Conclusion

This study explores the extent to which iron size distribution at emission, specifically from anthropogenic sources, alters estimates of soluble iron deposition to the open ocean. A global microphysical, size-resolved aerosol model is used to simulate the iron cycle, involving emission, atmospheric processing, and deposition on a global scale. The model treats iron mineralogy, size evolution, and chemical aging processes during atmospheric transport, which enables the investigation on the relationship between iron size distributions and iron long-range transport and subsequent deposition. We test four representative size distribution schemes for anthropogenic iron sources employed in previous studies.

We find that allocating a more balanced fraction of iron aerosol at emission into particle sizes less than $1 \mu\text{m}$, results in a longer atmospheric lifetime and mass burden of total iron aerosols by about a factor of 2 compared to a coarse-sized dominated case, primarily associated with the decreased loss rates via dry and wet removal processes. The evaluation of anthropogenic iron aerosols against the global-scale observation dataset reveals that despite the same emission fluxes considered in all cases, their simulated magnetite aerosol concentrations differ by up to a factor of 10, while the higher fine-sized cases agree better with the observations. It is therefore necessary to accurately represent iron size distributions in order to constrain iron emission fluxes more realistically with aerosol simulations and observations (Liu et al., 2022). Our simulations show that the resulting

343 annual soluble iron deposition differs by up to a factor of 1.5 over remote oceans including the North Pacific Ocean and
344 Southern Ocean, because the fine-sized group allows more iron to be transported to a long distance with enhanced atmospheric
345 processing. More importantly, the monthly soluble iron deposition, which is relevant to ocean primary production responses
346 over days to months, would be enhanced by 110% and 80% in the fine-sized case over the Southern Ocean and North Pacific
347 Ocean, respectively. Such differences are similar to or even larger than those with the consideration of emission uncertainty,
348 suggesting the equally important role of iron size distribution treatment.

349 This study unravels the critical role of iron size distributions in shaping atmospheric soluble iron inputs to global oceans,
350 especially to the remote regions. However, the realistic understanding of iron emission size distributions is still inadequate
351 given limited observation data. Targeted in-site measurements on iron aerosol size along with its mass and solubility at source
352 areas are highly desirable. [Higher resolution models with finer grids and detailed microphysics are useful to explore iron
353 aerosol deposition and chemical aging processes at regional scales.](#) Furthermore, our finding may be extended to other key
354 trace elements of importance to ocean biogeochemistry, like copper, manganese, and phosphorus.

355

356 **Competing interests:** The authors declare that they have no conflict of interest.

357 **Data availability:** The model data used to generate the figures can be available after the acceptance of the manuscript.

358 **Code availability:** The CESM source code is publicly available from NCAR at: <https://www.cesm.ucar.edu/>.

359 Acknowledgement

360 This study was supported by the Ministry of Education, Culture, Sports, Science, and Technology and the Japan Society for
361 the Promotion of Science (MEXT/JSPS) KAKENHI Grants (JP19H04253, JP19H05699, JP19KK0265, JP20H00196,
362 JP20H00638, JP22H03722, JP22F22092, JP23H00515, [JP23H00523](#), [JP23K18519](#), [JP23K24976](#), and
363 [JP24H02225](#)~~JP23H00523~~, and ~~JP23K18519~~); by the MEXT Arctic Challenge for Sustainability II (ArCS II) Project
364 (JPMXD1420318865); and by the Environment Research and Technology Development Fund 2–2003 (JPMEERF20202003)
365 and 2–2301 (JPMEERF20232001) of the Environmental Restoration and Conservation Agency. Mingxu Liu acknowledged
366 the support of JSPS Postdoctoral Fellowships for Research in Japan (Standard). DSH was supported by NASA (Proposal
367 Number: 22-IDS22-0027). We acknowledged the NASA Radiation Sciences Program, the NASA Upper Atmosphere Research
368 Program, and the NOAA Atmospheric Composition and Climate Program for providing the aircraft observational data.

369

370 References:

- 371 Albani, S., Mahowald, N. M., Perry, A. T., Scanza, R. A., Zender, C. S., Heavens, N. G., Maggi, V., Kok, J. F.,
372 and Otto-Bliesner, B. L.: Improved dust representation in the Community Atmosphere Model, *J. Adv. Model.*
373 *Earth Syst.*, 6, 541-570, <https://doi.org/10.1002/2013MS000279>, 2014.
- 374 Baldo, C., Ito, A., Krom, M. D., Li, W., Jones, T., Drake, N., Ignatyev, K., Davidson, N., and Shi, Z.: Iron from
375 coal combustion particles dissolves much faster than mineral dust under simulated atmospheric acidic
376 conditions, *Atmos. Chem. Phys.*, 22, 6045-6066, 10.5194/acp-22-6045-2022, 2022.
- 377 Bergas-Massó, E., Gonçalves Ageitos, M., Myriokefalitakis, S., Miller, R. L., van Noije, T., Le Sager, P., Montan
378 é Pinto, G., and Pérez García-Pando, C.: Pre-Industrial, Present and Future Atmospheric Soluble Iron
379 Deposition and the Role of Aerosol Acidity and Oxalate Under CMIP6 Emissions, *Earth's Future*, 11,
380 10.1029/2022ef003353, 2023.
- 381 Conway, T. M., Hamilton, D. S., Shelley, R. U., Aguilar-Islas, A. M., Landing, W. M., Mahowald, N. M., and John,
382 S. G.: Tracing and constraining anthropogenic aerosol iron fluxes to the North Atlantic Ocean using iron
383 isotopes, *Nat Commun*, 10, 2628, 10.1038/s41467-019-10457-w, 2019.

384 Gliß, J., Mortier, A., Schulz, M., Andrews, E., Balkanski, Y., Bauer, S. E., Benedictow, A. M. K., Bian, H., Checa-
385 Garcia, R., Chin, M., Ginoux, P., Griesfeller, J. J., Heckel, A., Kipling, Z., Kirkevåg, A., Kokkola, H., Laj, P.,
386 Le Sager, P., Lund, M. T., Lund Myhre, C., Matsui, H., Myhre, G., Neubauer, D., van Noije, T., North, P.,
387 Oliví, D. J. L., Rémy, S., Sogacheva, L., Takemura, T., Tsigaridis, K., and Tsyro, S. G.: AeroCom phase III
388 multi-model evaluation of the aerosol life cycle and optical properties using ground- and space-based remote
389 sensing as well as surface in situ observations, *Atmos. Chem. Phys.*, 21, 87-128, 10.5194/acp-21-87-2021,
390 2021.

391 Guieu, C., Aumont, O., Paytan, A., Bopp, L., Law, C. S., Mahowald, N., Achterberg, E. P., Marañón, E., Salihoglu,
392 B., Crise, A., Wagener, T., Herut, B., Desboeufs, K., Kanakidou, M., Olgun, N., Peters, F., Pulido-Villena, E.,
393 Tovar-Sanchez, A., and Völker, C.: The significance of the episodic nature of atmospheric deposition to Low
394 Nutrient Low Chlorophyll regions, *Global Biogeochemical Cycles*, 28, 1179-1198,
395 <https://doi.org/10.1002/2014GB004852>, 2014.

396 Hamilton, D. S., Scanza, R. A., Rathod, S. D., Bond, T. C., Kok, J. F., Li, L., Matsui, H., and Mahowald, N. M.:
397 Recent (1980 to 2015) Trends and Variability in Daily-to-Interannual Soluble Iron Deposition from Dust,
398 Fire, and Anthropogenic Sources, *Geophysical Research Letters*, 47, e2020GL089688,
399 10.1029/2020gl089688, 2020a.

400 Hamilton, D. S., Scanza, R. A., Feng, Y., Guinness, J., Kok, J. F., Li, L., Liu, X., Rathod, S. D., Wan, J. S., Wu,
401 M., and Mahowald, N. M.: Improved methodologies for Earth system modelling of atmospheric soluble iron
402 and observation comparisons using the Mechanism of Intermediate complexity for Modelling Iron (MIMI
403 v1.0), *Geosci. Model Dev.*, 12, 3835-3862, 10.5194/gmd-12-3835-2019, 2019.

404 Hamilton, D. S., Moore, J. K., Arneth, A., Bond, T. C., Carslaw, K. S., Hantson, S., Ito, A., Kaplan, J. O., Lindsay,
405 K., Nieradzick, L., Rathod, S. D., Scanza, R. A., and Mahowald, N. M.: Impact of Changes to the Atmospheric
406 Soluble Iron Deposition Flux on Ocean Biogeochemical Cycles in the Anthropocene, *Global Biogeochemical
407 Cycles*, 34, e2019GB006448, 10.1029/2019gb006448, 2020b.

408 Hamilton, D. S., Perron, M. M. G., Bond, T. C., Bowie, A. R., Buchholz, R. R., Guieu, C., Ito, A., Maenhaut, W.,
409 Myriokefalitakis, S., Olgun, N., Rathod, S. D., Schepanski, K., Tagliabue, A., Wagner, R., and Mahowald, N.
410 M.: Earth, Wind, Fire, and Pollution: Aerosol Nutrient Sources and Impacts on Ocean Biogeochemistry, 14,
411 303-330, 10.1146/annurev-marine-031921-013612, 2022.

412 Ito, A.: Global modeling study of potentially bioavailable iron input from shipboard aerosol sources to the ocean,
413 *Global Biogeochemical Cycles*, 27, 1-10, <https://doi.org/10.1029/2012GB004378>, 2013.

414 Ito, A.: Atmospheric Processing of Combustion Aerosols as a Source of Bioavailable Iron, *Environ. Sci. Technol.
415 Lett.*, 2, 70-75, 10.1021/acs.estlett.5b00007, 2015.

416 Ito, A., Ye, Y., Yamamoto, A., Watanabe, M., and Aita, M. N.: Responses of ocean biogeochemistry to atmospheric
417 supply of lithogenic and pyrogenic iron-containing aerosols, *Geol. Mag.*, 157, 741-756,
418 10.1017/S0016756819001080, 2020.

419 Ito, A., Myriokefalitakis, S., Kanakidou, M., Mahowald, N. M., Scanza, R. A., Hamilton, D. S., Baker, A. R.,
420 Jickells, T., Sarin, M., Bikkina, S., Gao, Y., Shelley, R. U., Buck, C. S., Landing, W. M., Bowie, A. R., Perron,
421 M. M. G., Guieu, C., Meskhidze, N., Johnson, M. S., Feng, Y., Kok, J. F., Nenes, A., and Duce, R. A.:
422 Pyrogenic iron: The missing link to high iron solubility in aerosols, *Sci. Adv.*, 5, eaau7671,
423 10.1126/sciadv.aau7671, 2019.

424 Jickells, T. and Moore, C. M.: The Importance of Atmospheric Deposition for Ocean Productivity, *Annu. Rev.
425 Ecol. Evol. Syst.*, 46, 481-501, 10.1146/annurev-ecolsys-112414-054118, 2015.

426 Jickells, T. D., An, Z. S., Andersen, K. K., Baker, A. R., Bergametti, G., Brooks, N., Cao, J. J., Boyd, P. W., Duce,
427 R. A., Hunter, K. A., Kawahata, H., Kubilay, N., laRoche, J., Liss, P. S., Mahowald, N., Prospero, J. M.,
428 Ridgwell, A. J., Tegen, I., and Torres, R.: Global Iron Connections Between Desert Dust, Ocean
429 Biogeochemistry, and Climate, *Science*, 308, 67, 10.1126/science.1105959, 2005.

430 Kawai, K., Matsui, H., and Tobo, Y.: High Potential of Asian Dust to Act as Ice Nucleating Particles in Mixed-
431 Phase Clouds Simulated With a Global Aerosol-Climate Model, *J. Geophys. Res.-Atmos*, 126,
432 e2020JD034263, <https://doi.org/10.1029/2020JD034263>, 2021.

433 Kok, J. F.: A scaling theory for the size distribution of emitted dust aerosols suggests climate models underestimate
434 the size of the global dust cycle, *Proceedings of the National Academy of Sciences of the United States of
435 America*, 108, 1016, 10.1073/pnas.1014798108, 2011.

436 Lamb, K. D., Matsui, H., Katich, J. M., Perring, A. E., Spackman, J. R., Weinzierl, B., Dollner, M., and Schwarz,
437 J. P.: Global-scale constraints on light-absorbing anthropogenic iron oxide aerosols, *npj Clim. Atmos. Sci.*, 4,
438 10.1038/s41612-021-00171-0, 2021.

439 Li, W., Xu, L., Liu, X., Zhang, J., Lin, Y., Yao, X., Gao, H., Zhang, D., Chen, J., Wang, W., Harrison, R. M.,
440 Zhang, X., Shao, L., Fu, P., Nenes, A., and Shi, Z.: Air pollution–aerosol interactions produce more
441 bioavailable iron for ocean ecosystems, *Sci. Adv.*, 3, e1601749, 10.1126/sciadv.1601749, 2017.

442 Liu, M. and Matsui, H.: Improved Simulations of Global Black Carbon Distributions by Modifying Wet
443 Scavenging Processes in Convective and Mixed-Phase Clouds, *J. Geophys. Res.-Atmos*, 126, e2020JD033890,
444 <https://doi.org/10.1029/2020JD033890>, 2021.

445 Liu, M. and Matsui, H.: Secondary Organic Aerosol Formation Regulates Cloud Condensation Nuclei in the Global
446 Remote Troposphere, *Geophysical Research Letters*, 49, 10.1029/2022gl100543, 2022.

447 Liu, M., Matsui, H., Hamilton, D. S., Lamb, K. D., Rathod, S. D., Schwarz, J. P., and Mahowald, N. M.: The
448 underappreciated role of anthropogenic sources in atmospheric soluble iron flux to the Southern Ocean, *npj*
449 *Clim. Atmos. Sci.*, 5, 10.1038/s41612-022-00250-w, 2022.

450 Liu, X., Easter, R. C., Ghan, S. J., Zaveri, R., Rasch, P., Shi, X., Lamarque, J. F., Gettelman, A., Morrison, H., Vitt,
451 F., Conley, A., Park, S., Neale, R., Hannay, C., Ekman, A. M. L., Hess, P., Mahowald, N., Collins, W., Iacono,
452 M. J., Bretherton, C. S., Flanner, M. G., and Mitchell, D.: Toward a minimal representation of aerosols in
453 climate models: description and evaluation in the Community Atmosphere Model CAM5, *Geosci. Model Dev.*,
454 5, 709-739, 10.5194/gmd-5-709-2012, 2012.

455 Longo, A. F., Feng, Y., Lai, B., Landing, W. M., Shelley, R. U., Nenes, A., Mihalopoulos, N., Violaki, K., and
456 Ingall, E. D.: Influence of Atmospheric Processes on the Solubility and Composition of Iron in Saharan Dust,
457 *Environmental Science & Technology*, 50, 6912-6920, 10.1021/acs.est.6b02605, 2016.

458 Luo, C., Mahowald, N., Bond, T., Chuang, P. Y., Artaxo, P., Siefert, R., Chen, Y., and Schauer, J.: Combustion
459 iron distribution and deposition, *Global Biogeochemical Cycles*, 22, GB1012,
460 <https://doi.org/10.1029/2007GB002964>, 2008.

461 Mahowald, N., Albani, S., Kok, J. F., Engelstaeder, S., Scanza, R., Ward, D. S., and Flanner, M. G.: The size
462 distribution of desert dust aerosols and its impact on the Earth system, *Aeolian Res.*, 15, 53-71,
463 <https://doi.org/10.1016/j.aeolia.2013.09.002>, 2014.

464 Mahowald, N. M., Hamilton, D. S., Mackey, K. R. M., Moore, J. K., Baker, A. R., Scanza, R. A., and Zhang, Y.:
465 Aerosol trace metal leaching and impacts on marine microorganisms, *Nat. Commun.*, 9, 2614,
466 10.1038/s41467-018-04970-7, 2018.

467 Mahowald, N. M., Engelstaeder, S., Luo, C., Sealy, A., Artaxo, P., Benitez-Nelson, C., Bonnet, S., Chen, Y.,
468 Chuang, P. Y., Cohen, D. D., Dulac, F., Herut, B., Johansen, A. M., Kubilay, N., Losno, R., Maenhaut, W.,
469 Paytan, A., Prospero, J. M., Shank, L. M., and Siefert, R. L.: Atmospheric Iron Deposition: Global Distribution,
470 Variability, and Human Perturbations, *Annual Review of Marine Science*, 1, 245-278,
471 10.1146/annurev.marine.010908.163727, 2009.

472 Matsui, H.: Development of a global aerosol model using a two-dimensional sectional method: 1. Model design, *J.*
473 *Adv. Model. Earth Syst.*, 9, 1921-1947, 10.1002/2017ms000936, 2017.

474 Matsui, H. and Liu, M.: Importance of Supersaturation in Arctic Black Carbon Simulations, *Journal of Climate*, 34,
475 7843-7856, 10.1175/jcli-d-20-0994.1, 2021.

476 Matsui, H. and Mahowald, N.: Development of a global aerosol model using a two-dimensional sectional method:
477 2. Evaluation and sensitivity simulations, *J. Adv. Model. Earth Syst.*, 9, 1887-1920, 10.1002/2017ms000937,
478 2017.

479 Matsui, H. and Moteki, N.: High sensitivity of Arctic black carbon radiative effects to subgrid vertical velocity in
480 aerosol activation, *Geophysical Research Letters*, 47, e2020GL088978, 10.1029/2020GL088978, 2020.

481 Matsui, H., Mori, T., Ohata, S., Moteki, N., Oshima, N., Goto-Azuma, K., Koike, M., and Kondo, Y.: Contrasting
482 source contributions of Arctic black carbon to atmospheric concentrations, deposition flux, and atmospheric
483 and snow radiative effects, *Atmos. Chem. Phys. Discuss.*, 2022, 1-31, 10.5194/acp-2021-1091, 2022.

484 Matsui, H., Mahowald, N. M., Moteki, N., Hamilton, D. S., Ohata, S., Yoshida, A., Koike, M., Scanza, R. A., and
485 Flanner, M. G.: Anthropogenic combustion iron as a complex climate forcer, *Nat. Commun.*, 9, 1593,
486 10.1038/s41467-018-03997-0, 2018.

487 Meskhidze, N., Völker, C., Al-Abadleh, H. A., Barbeau, K., Bressac, M., Buck, C., Bundy, R. M., Croot, P., Feng,
488 Y., Ito, A., Johansen, A. M., Landing, W. M., Mao, J., Myriokefalitakis, S., Ohnemus, D., Pasquier, B., and
489 Ye, Y.: Perspective on identifying and characterizing the processes controlling iron speciation and residence
490 time at the atmosphere-ocean interface, *Marine Chemistry*, 217, 103704,
491 <https://doi.org/10.1016/j.marchem.2019.103704>, 2019.

492 Moore, C. M., Mills, M. M., Arrigo, K. R., Berman-Frank, I., Bopp, L., Boyd, P. W., Galbraith, E. D., Geider, R.
493 J., Guieu, C., Jaccard, S. L., Jickells, T. D., La Roche, J., Lenton, T. M., Mahowald, N. M., Marañón, E.,
494 Marinov, I., Moore, J. K., Nakatsuka, T., Oschlies, A., Saito, M. A., Thingstad, T. F., Tsuda, A., and Ulloa,
495 O.: Processes and patterns of oceanic nutrient limitation, *Nat. Geosci.*, 6, 701-710, 10.1038/ngeo1765, 2013.

496 Moore, J. K., Doney, S. C., Glover, D. M., and Fung, I. Y.: Iron cycling and nutrient-limitation patterns in surface
497 waters of the World Ocean, *Deep Sea Research Part II: Topical Studies in Oceanography*, 49, 463-507,
498 [https://doi.org/10.1016/S0967-0645\(01\)00109-6](https://doi.org/10.1016/S0967-0645(01)00109-6), 2001.

499 Moteki, N., Adachi, K., Ohata, S., Yoshida, A., Harigaya, T., Koike, M., and Kondo, Y.: Anthropogenic iron oxide
500 aerosols enhance atmospheric heating, *Nat. Commun.*, 8, 15329, [10.1038/ncomms15329](https://doi.org/10.1038/ncomms15329), 2017.

501 Myriokefalitakis, S., Gröger, M., Hieronymus, J., and Döscher, R.: An explicit estimate of the atmospheric nutrient
502 impact on global oceanic productivity, *Ocean Sci.*, 16, 1183-1205, [10.5194/os-16-1183-2020](https://doi.org/10.5194/os-16-1183-2020), 2020.

503 Myriokefalitakis, S., Ito, A., Kanakidou, M., Nenes, A., Krol, M. C., Mahowald, N. M., Scanza, R. A., Hamilton,
504 D. S., Johnson, M. S., Meskhidze, N., Kok, J. F., Guieu, C., Baker, A. R., Jickells, T. D., Sarin, M. M., Bikkina,
505 S., Shelley, R., Bowie, A., Perron, M. M. G., and Duce, R. A.: Reviews and syntheses: the GESAMP
506 atmospheric iron deposition model intercomparison study, *Biogeosciences*, 15, 6659-6684, [10.5194/bg-15-6659-2018](https://doi.org/10.5194/bg-15-6659-2018), 2018.

508 Okin, G. S., Baker, A. R., Tegen, I., Mahowald, N. M., Dentener, F. J., Duce, R. A., Galloway, J. N., Hunter, K.,
509 Kanakidou, M., Kubilay, N., Prospero, J. M., Sarin, M., Surapipith, V., Uematsu, M., and Zhu, T.: Impacts of
510 atmospheric nutrient deposition on marine productivity: Roles of nitrogen, phosphorus, and iron, *Global
511 Biogeochemical Cycles*, 25, <https://doi.org/10.1029/2010GB003858>, 2011.

512 Rathod, S. D., Hamilton, D. S., Mahowald, N. M., Klimont, Z., Corbett, J. J., and Bond, T. C.: A Mineralogy-
513 Based Anthropogenic Combustion-Iron Emission Inventory, *J. Geophys. Res.-Atmos*, 125, e2019JD032114,
514 [10.1029/2019jd032114](https://doi.org/10.1029/2019jd032114), 2020.

515 Rathod, S. D., Hamilton, D. S., Li, L., Mahowald, N. M., Matsui, H., Pierce, J. R., and Bond, T. C.: Atmospheric
516 Radiative and Oceanic Biological Productivity Responses to Increasing Anthropogenic Combustion-Iron
517 Emission in the 1850–2010 Period, *Geophys. Res. Lett.*, 49, [10.1029/2022gl099323](https://doi.org/10.1029/2022gl099323), 2022.

518 Seo, H. and Kim, G.: Anthropogenic Iron Invasion into the Ocean: Results from the East Sea (Japan Sea), *Environ.
519 Sci. Technol.*, 57, 10745-10753, [10.1021/acs.est.3c01084](https://doi.org/10.1021/acs.est.3c01084), 2023.

520 Shi, J., Guan, Y., Ito, A., Gao, H., Yao, X., Baker, A. R., and Zhang, D.: High Production of Soluble Iron Promoted
521 by Aerosol Acidification in Fog, *Geophysical Research Letters*, 47, [10.1029/2019gl086124](https://doi.org/10.1029/2019gl086124), 2020.

522 Shi, Z., Krom, M. D., Jickells, T. D., Bonneville, S., Carslaw, K. S., Mihalopoulos, N., Baker, A. R., and Benning,
523 L. G.: Impacts on iron solubility in the mineral dust by processes in the source region and the atmosphere: A
524 review, *Aeolian Res.*, 5, 21-42, <https://doi.org/10.1016/j.aeolia.2012.03.001>, 2012.

525 Solmon, F., Chuang, P. Y., Meskhidze, N., and Chen, Y.: Acidic processing of mineral dust iron by anthropogenic
526 compounds over the north Pacific Ocean, *J. Geophys. Res.-Atmos*, 114,
527 <https://doi.org/10.1029/2008JD010417>, 2009.

528 Tagliabue, A., Bowie, A. R., Boyd, P. W., Buck, K. N., Johnson, K. S., and Saito, M. A.: The integral role of iron
529 in ocean biogeochemistry, *Nature*, 543, 51-59, [10.1038/nature21058](https://doi.org/10.1038/nature21058), 2017.

530 Wang, R., Balkanski, Y., Boucher, O., Bopp, L., Chappell, A., Ciais, P., Hauglustaine, D., Peñuelas, J., and Tao,
531 S.: Sources, transport and deposition of iron in the global atmosphere, *Atmos. Chem. Phys.*, 15, 6247-6270,
532 [10.5194/acp-15-6247-2015](https://doi.org/10.5194/acp-15-6247-2015), 2015.

533 Westberry, T. K., Behrenfeld, M. J., Shi, Y. R., Yu, H., Remer, L. A., and Bian, H.: Atmospheric nourishment of
534 global ocean ecosystems, 380, 515-519, [doi:10.1126/science.abq5252](https://doi.org/10.1126/science.abq5252), 2023.

535 Zender, C. S., Bian, H., and Newman, D.: Mineral Dust Entrainment and Deposition (DEAD) model: Description
536 and 1990s dust climatology, *J. Geophys. Res.-Atmos*, 108, 4416, <https://doi.org/10.1029/2002JD002775>,
537 2003.

538 Zhang, H., Li, R., Dong, S., Wang, F., Zhu, Y., Meng, H., Huang, C., Ren, Y., Wang, X., Hu, X., Li, T., Peng, C.,
539 Zhang, G., Xue, L., Wang, X., and Tang, M.: Abundance and Fractional Solubility of Aerosol Iron During
540 Winter at a Coastal City in Northern China: Similarities and Contrasts Between Fine and Coarse Particles, *J.
541 Geophys. Res.-Atmos*, 127, e2021JD036070, <https://doi.org/10.1029/2021JD036070>, 2022.

542 Zhang, H., Li, R., Huang, C., Li, X., Dong, S., Wang, F., Li, T., Chen, Y., Zhang, G., Ren, Y., Chen, Q., Huang,
543 R., Chen, S., Xue, T., Wang, X., and Tang, M.: Seasonal variation of aerosol iron solubility in coarse and fine
544 particles at an inland city in northwestern China, *Atmos. Chem. Phys.*, 23, 3543-3559, [10.5194/acp-23-3543-2023](https://doi.org/10.5194/acp-23-3543-2023), 2023.

546 Zhang, L., Gong, S., Padro, J., and Barrie, L.: A size-segregated particle dry deposition scheme for an atmospheric
547 aerosol module, *Atmospheric Environment*, 35, 549-560, [https://doi.org/10.1016/S1352-2310\(00\)00326-5](https://doi.org/10.1016/S1352-2310(00)00326-5),
548 2001.

549 Zhu, Y., Li, W., Wang, Y., Zhang, J., Liu, L., Xu, L., Xu, J., Shi, J., Shao, L., Fu, P., Zhang, D., and Shi, Z.: Sources
550 and processes of iron aerosols in a megacity in Eastern China, *Atmos. Chem. Phys.*, 22, 2191-2202,
551 [10.5194/acp-22-2191-2022](https://doi.org/10.5194/acp-22-2191-2022), 2022.

552